Impedance spectroscopy study of $SrTiO_3$ pulse laser deposited photoelectrodes

Robert W. Call[a], Shane Brogan[b], Leila Alibabaei[c], Rene Lopez[a*]

Affiliations

[a]Department of Physics and Astronomy, University of North Carolina at Chapel Hill, Chapel Hill, North Carolina 27599, United States.

[b]Department of Applied Sciences, University of North Carolina at Chapel Hill, Chapel Hill, North Carolina 27599, United States.

[c]Department of Chemistry, University of North Carolina at Chapel Hill, Chapel Hill, North Carolina 27599, United States.

*Corresponding Author. E-mail address rln@email.unc.edu

Abstract

Strontium titanate (STO) is an oxide that has found application in several technological areas and is a candidate electrode for photoelectrochemical cells (PECs). In this study, STO thin films were prepared via pulsed laser deposition to function as PEC electrodes. Effects of post-deposition annealing in a reducing environment on the photocatalytic activity of these electrodes are characterized by measurements of optical and electrochemical properties of the films. These observations are used to obtain insight into how the crystal and electronic properties of these electrodes are affected by the annealing process. Low annealing temperatures produce non-crystalline STO films that exhibit low photocatalytic activity. Annealing at 500 °C and higher allowed the formation of crystalline STO, which showed substantially higher ultraviolet-driven photocurrent densities. Electrochemical impedance spectroscopy reveals large decreases in charge transfer resistance that are associated with improved performance of these films. Oxygen evolution at these electrodes was confirmed with a rotating ring-disk electrode setup. Porous versions of the STO films were investigated to evaluate the effect larger surface area can have in enhancing the water oxidation performance.

Keywords: Strontium titanate; Photoelectrochemical cells; Electrochemical impedance spectroscopy; Spectroscopic ellipsometry; Pulsed laser deposition.

1. Introduction

Photoelectrochemical cells (PECs) provide a potential solution to some of the fundamental problems faced by solar power, particularly its variability. By using solar radiation to create a fuel, PECs could effectively bottle solar energy allowing it to be shipped and used wherever and whenever it is needed. Various architectures and fuel products have been proposed for PECs. This work is concerned with water-splitting via an illuminated, semiconductor photoanode that drives oxygen evolution in series with a dark electrode that catalyzes hydrogen evolution. The properties of the semiconductor electrode play an essential role in the performance of the PEC. Optical bandgap, band-edge positions, electrochemical stability, and dielectric properties of the material are particularly important for sustaining the reaction. Due to their properties, several metal-oxide semiconductors have been considered for constructing photoanodes for PECs.

Strontium titanate (STO) has been investigated for use in these electrodes because of its high electrochemical stability. Single-crystal STO was first used for photoelectrochemical applications in the 1970's and had the distinction of catalyzing a water-splitting reaction with no external applied bias [1,2]. Single-crystal STO has been investigated as a photoelectrode in a variety of studies [1–6] as has STO in thin film forms [7–13]. Its band structure and dielectric properties are however not ideal for water-splitting, and their tuning via doping remains a topic of interest. The simplest methods for doping STO are accomplished during the growth process or through a post-growth annealing step. In earlier work with single-crystal bulk STO, electrodes are often annealed at temperatures ranging from 800 °C to 1100 °C in hydrogen atmospheres to improve its charge density and electrical conductivity. Annealing temperatures

reported in literature for STO thin film photoelectrodes range from 450 °C to 1100 °C. Notably, high temperature anneals in reducing environments have been shown to create oxygen vacancies in the STO lattice resulting in electron donor states and increased conductivity [14,15]. There is some evidence that interstitial hydrogen doping also occurs during these anneals and creates shallow donor states [15,16].

The annealing conditions for STO films have been shown to influence crystallinity, band-structure, dielectric properties, and optical properties of STO films [14,15,17–28], all important factors on the photocatalytic performance of STO photoanodes. Nevertheless, published accounts on the photocatalytic properties of reduced STO films lack methodical studies of annealing temperature effects but instead have focused on alternative doping strategies (other metal impurities) or unassociated electrode properties (ie. adsorbed catalyst). In a previous investigation we showed the effects of annealing in different environments (atmosphere, O_2, H_2/Ar) on STO electrodes specifically for dye-sensitized PECs [29]. In that case, the study of performance change with annealing temperature was limited by the substrate stability – i.e. transparent fluorine doped tin oxide.

Below we present a systematic study on the effects of post-deposition annealing temperature on two properties of STO films that strongly effect their performance as PEC photoanodes, namely optical bandgap and electrical impedance. A pure titanium substrate is employed allowing STO films to be annealed at higher temperatures than conventional STO thin films in literature. We have found that higher annealing temperatures are correlated with lower electrical impedance and narrower optical bandgaps in STO films, and furthermore these changes are associated with large improvements in performance for these films as PEC photoanodes under ultraviolet (UV) illumination. We have also identified a minimum temperature requirement for

the annealing step to achieve STO films that exhibit band structures similar to single-crystal STO. In this investigation, both flat and porous films were fabricated under similar conditions and tested to investigate the role of the electrode morphology in electrochemical performance. This work definitively shows how the material physical property changes correlate to improvements in photocatalytic performance of STO films.

2. Experimental Details

STO films were grown with a PVD Products pulsed laser deposition system (NanoPLD) at room temperature from a sintered STO target (PVD Products, 99.9% pure). Titanium substrates were used for electrochemical measurements while silicon and fused silica were used to create twin samples for optical measurements. An O_2 back pressure of 1 Pa was used to make flat, dense films. Porous films were grown by depositing first a 20 nm flat, dense film and then proceeding with porous growth at 30 Pa O_2 back pressure. The dense underlayer was used to ensure the Ti substrate could not have direct contact with the electrolyte during the photoelectrochemical experiments. Post-deposition annealing was done in a 2.5% hydrogen (balance gas argon) atmosphere using an MTI Corporation OTF-1200X tube furnace. Post-deposition annealing temperatures varied from 300 °C to 700 °C for different samples with the temperature being maintained for two hours.

Prior to selecting titanium metal as the substrate, we noted that high temperature anneals in a 2.5% hydrogen atmosphere dramatically decreased the conductivity of a number of substrates considered for this study. Fluorine-doped tin-oxide, silver foil, glassy carbon, and high-conductivity silicon (As-doped) were all degraded under this reducing atmosphere. The titanium substrate proved to be the best though it also showed increased (x100) resistivity at annealing temperatures ≥700 °C, presumably from a surface reaction/compositional alteration. This

change in conductivity for anneals at 700 °C was also eliminated by coating the metal substrate with Al_2O_3, before STO film deposition, on all sides except the side that supports the STO film. Al_2O_3 deposition was done via atomic layer deposition. It was found that a 10 nm thick Al_2O_3 coating was sufficient to prevent increases in substrate resistivity on the back side of the substrate.

Spectroscopic optical characterizations were made with two different techniques. A J.A. Woollam V-Vase spectroscopic ellipsometer with an HS-190 monochromator light-source was used to determine optical constants by fitting data to a multi-oscillator model (J.A. Woollam, W-Vase software). A custom setup incorporating a light source (Spectral Products, ASBN-W series) integrating sphere (Labsphere), and monochromater (SpetraPro) was used to independently determine the film absorption. Samples for spectroscopic ellipsometry and reflection measurements were grown on silicon wafer substrates (100). Samples for absorption measurements were deposited on fused silica. X-ray diffraction (XRD) measurements were performed with a Rigaku SmartLab X-Ray Diffractometer (Cu source, 1.5418 Å, 0.02 ^{o}/s) for STO films on fused silica. Samples on the titanium substrates were too small for the XRD spot size to obtain reliable data but could have produced Ti-rich STO films.

Electrochemical impedance spectroscopy (EIS) curves and UV-illuminated photocurrents were measured using a Rotating Ring-Disk Electrode (RRDE) setup (Pine Instruments AFMSRCE) with the disk electrode replaced by the titanium substrate. A platinum wire counter electrode and double-junction Ag/AgCl reference electrode were used to complete the electrochemical cell. In the case of RRDE a platinum ring electrode surrounds the disk electrode. Current at the ring electrode is monitored for changes correlated to illumination of the disk working electrode. The platinum ring electrode had no applied bias for these experiments

except in the case of oxygen measurements via RRDE. Electrolyte for photocurrent measurements was at pH 5.8 with 0.2 M $LiClO_4$ in an acetate buffer. A CH Instruments Model 760E Bipotentiostat was used to collect electrochemical data. EIS curves were taken with a voltage oscillation amplitude of ±5 mV at twelve points per decade frequency. When a potential bias was used with EIS measurements the system was allowed to equilibrate before

For porous films it was preferable to make films as thick as possible to maximize surface area while maintaining structural integrity. To meet both requirements porous films were grown to 650 nm total thickness. As porous electrodes have delicate 3D structures that can be damaged by loading into the RRDE setup, electrodes for these films were constructed by connecting the titanium substrate to a wire using a conductive epoxy (Chemtronics CW2400) and then covering the connection and exposed titanium with a stable, electrically resistive epoxy (Hysol E-00CL). Flat films on Ti substrates were also made into electrodes with this technique to obtain comparable measurements.

Illumination for electrochemical measurements was provided by a continuous wave solid-state laser from Crystal Laser with 375 nm wavelength. Light intensity was controlled by adjusting laser-to-sample distance and with neutral density filters. For measurements in the RRDE setup laser intensity at the sample was approximately 4.0 ± 0.1 mW/cm^2 while measurements in the sealed cell had intensity 1.7 ± 0.1 mW/cm^2 at the sample.

3. Results and Discussion

3.1. Photocurrent Measurements

Initially we considered a possible relationship between film thickness and photocurrent generation, therefore a series of films were created ranging from 20 nm to 1 μm thick and post-

annealed at 700 °C. The results, summarized in Figure 1.a, show that photocurrent slightly peaked at a thickness of 40 nm. The underlying cause of this peak performance at 40 nm thickness is not obvious, as optical absorption and electrical resistance could both be functions of the geometric dimensions. Electrochemical impedance spectroscopy was used to examine these films. EIS on illuminated films showed only small differences in impedance for films of different thickness (Figure 1.b). Given the photocurrents were all also within a factor of two from each other, this is a relatively small effect compared to what will be shown results from the annealing conditions (below), therefore we conclude that film thickness in the explored range did not have a substantial effect on performance. The 40 nm thickness was maintained for the subsequent investigations into annealing effects.

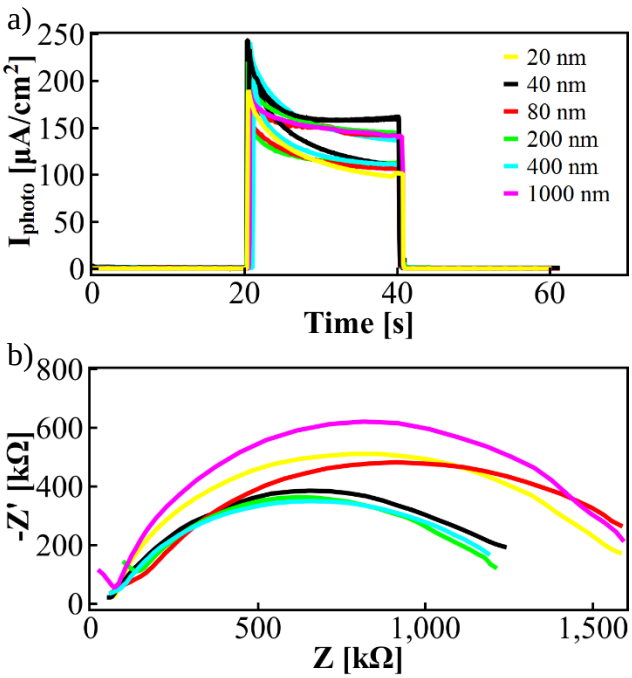

Figure 1. a) Photocurrent data for several thicknesses. b) EIS data (illuminated) for these thicknesses.

Photocurrent measurements of these films under the conditions described above were done for films annealed at several temperature setpoints. Figure 2 shows that films annealed up-to and below 300 °C exhibited < 0.1 μA/cm^2 photocurrent densities. Annealing above that point resulted in significant improvements in photocurrent densities, with a ~10^4 factor increase for the best film which was annealed at 700 ℃. Incident photon-to-electron conversion efficiency (IPCE) for the film annealed at 700 ^{o}C under these conditions (0V bias vs. Ag/AgCl, 375 nm, 4.0 mW/cm^2) is 67%. True IPCE is measured under short circuit conditions, for these films with applied bias of 0 V vs. a normal hydrogen electrode the IPCE was 28%.

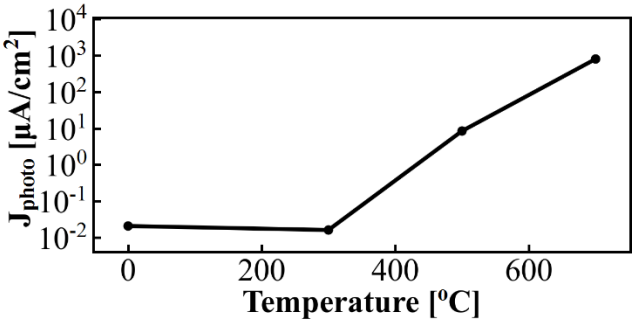

Figure 2. Plot of measured photocurrent density for STO films with increasing annealing temperature with 0 V applied bias vs. Ag/AgCl. Photocurrents were measured by subtracting the dark current from the measured photocurrent 20 seconds after illumination to allow the system to come to equilibrium.

The cause for this dramatic increase in photocurrent for films annealed at higher temperatures is the subject under investigation below. Along with photocurrent measurements, spectroscopic ellipsometry and EIS are used to investigate what the underlying cause of this large increase in performance might be.

3.2. XRD and Optical Characterization

Film crystallinity is expected to play a very important role in the large photocurrent density changes noted in Figure 2. Figure 3 shows the clear XRD signature of an STO film annealed at 700 °C. XRD data shows that STO films annealed (at or beyond 500 °C) via the same methodology and parameters described here indeed result in films with the same crystal spacings [29]. Films annealed at or below 300 °C did not exhibit STO peaks (see Figure 3.b for comparison). These differences in film crystallinity have an impact on the electronic properties of the films, however, it is not the only important factor as will be shown in detail in the Section 3.3.

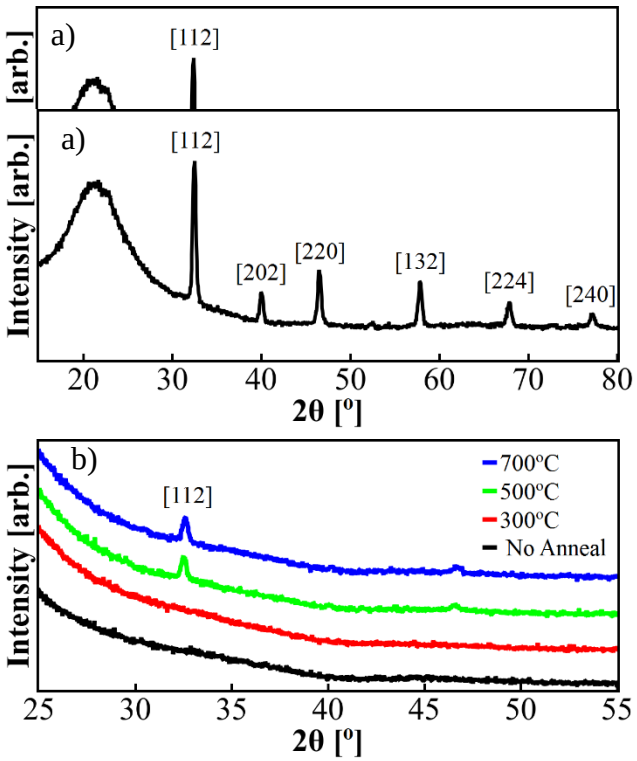

Figure 3. a) XRD patterns of STO film annealed at 700 °C. The broad peak at 20° is from the fused silica substrate. b) XRD patterns from fast scans of STO films on fused silica annealed at different temperatures.

For these thin films differences in absorption were studied by examining the extinction coefficient spectra of the films via ellipsometry. In order to obtain extinction coefficients for these films, fits to a multi-oscillator model were performed from the ellipsometric and reflection data. The films were characterized with the ellipsometer using a range of wavelengths from 300 nm – 1000 nm and examined at 65°, 70°, and 75° incidence angles. Reflection measurements were taken at 20°, 30°, and 40°. Films that were annealed at > 500 °C were closely modeled by a Tauc-Lorentz oscillator, a standard semiconductor model. Unannealed films and films annealed at 300 °C required a combination of a Tauc-Lorentz and a Gaussian oscillator (commonly used to fit insulating or amorphous films). Extinction coefficients (k) and index of refraction calculations (n) are shown in Figure 4 along with the ellipsometric data and fits described above.

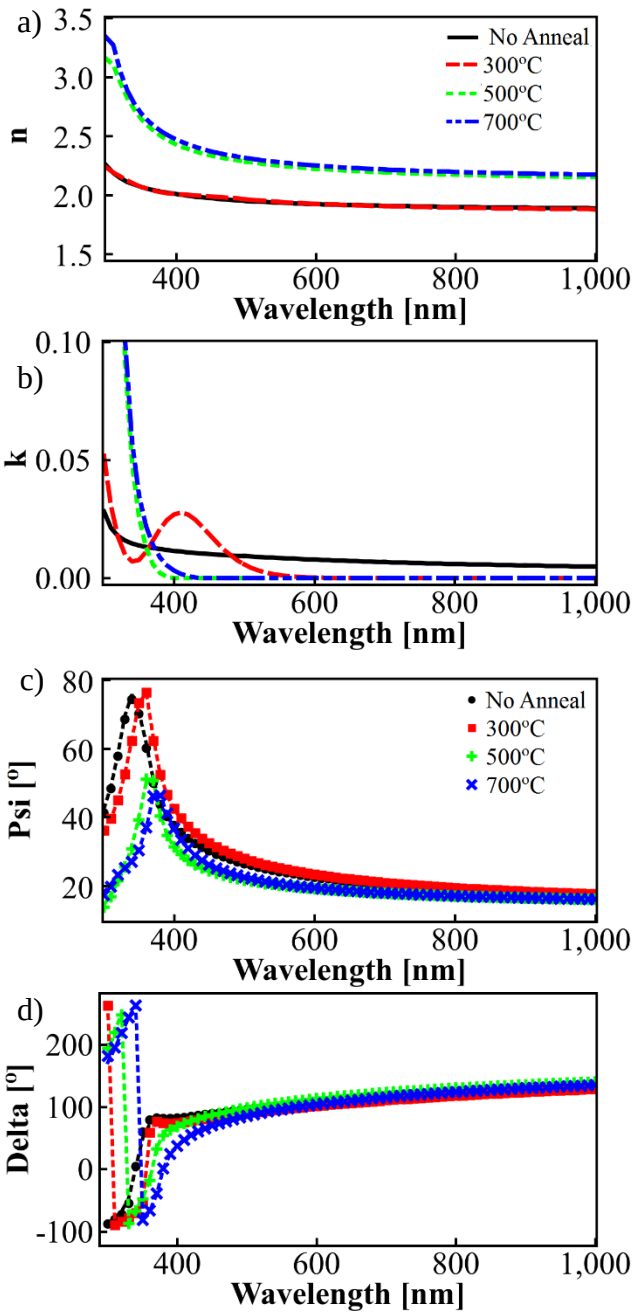

Figure 4. a) Index of refraction of all samples vs. wavelength. b) Extinction coefficients for all samples. Raw data from ellipsometry appears in (c) and (d), psi and delta respectively. Fits to the raw data are shown as dashed lines of the same color.

Significant changes were found for both n and k values for films annealed at different temperatures. Samples annealed at a minimum of 500 °C show a distinct difference from samples annealed at lower temperatures. Films annealed at 500 °C or higher were within 10 % of the index of refraction of single-crystal STO (n = 2.4 over the visible range). The unannealed films and films annealed at 300 °C differed from single-crystal by more than 20 %. While differences in index of refraction for samples annealed at 500 °C and 700 °C are minimal that is not true for their extinction coefficients. Extinction coefficient spectra show that the 700 °C samples have a higher concentration of donor states than 500 °C samples leading to an apparent downshift of the bend edge. The band gap for films annealed at 500 °C appears near 380 nm (k > 0.001) which corresponds closely to previous measurements of the indirect band gap of bulk STO [30]. Films annealed at 700 °C begin to absorb at 420 nm indicating a 0.3 eV diminution of the bandgap. At 375 nm wavelength (the illumination wavelength for electrochemical the experiments), the extinction coefficients for samples annealed at 700 °C are 60% higher than samples annealed at 500 °C indicating that the 700 °C samples will absorb slightly more light for these experiments. Taken together these results show that while there is only a small difference in crystallinity for films annealed at 500 °C and 700 °C, there must be a significant difference in donor states. However, the enhanced absorption is not sufficient to explain the large ~100 fold photocurrent jump between those two annealing conditions. Changes in electric charge transport properties should still be the main factor behind the improvements.

3.3. Electrochemical Impedance Spectroscopy

The process of annealing these electrodes in a reducing environment should create donor states near the conduction band edge. As seen above, a sufficient number of these states significantly changes the band edges of the STO. In a PEC the band edges of the semiconductor

electrode need to be properly aligned with the redox potentials of the electroactive species. Charge needs to be efficiently transferred into the film and passed to the conductive substrate without significant recombination back into the electrolyte. Impedance measurements of the system can provide insight into how the changes in the band edges are affecting the performance of these films. They can also reveal any changes in the dielectric properties of the film. Here duplicate films annealed at different temperatures were investigated with EIS to characterize any changes in impedance due to annealing temperature. Samples were tested under 0 V applied bias vs. Ag/AgCl with an illumination bias as recommended by Adachi et al. [31]. By operating under an illumination bias EIS data will reveal more about the processes occurring when the system is under operating conditions.

Figure 5 shows that the impedance of these STO films changes significantly with the post-deposition annealing temperature. The variation in impedance between unannealed samples and samples annealed at 700 °C is nearly a factor of 10^4. These large changes in impedance point to significant reductions in charge-transfer resistance and bulk resistance. We note that electrolyte was constant throughout these measurements limiting the possible causes for these changes to shifts in the band structure and charge transport properties of these electrodes.

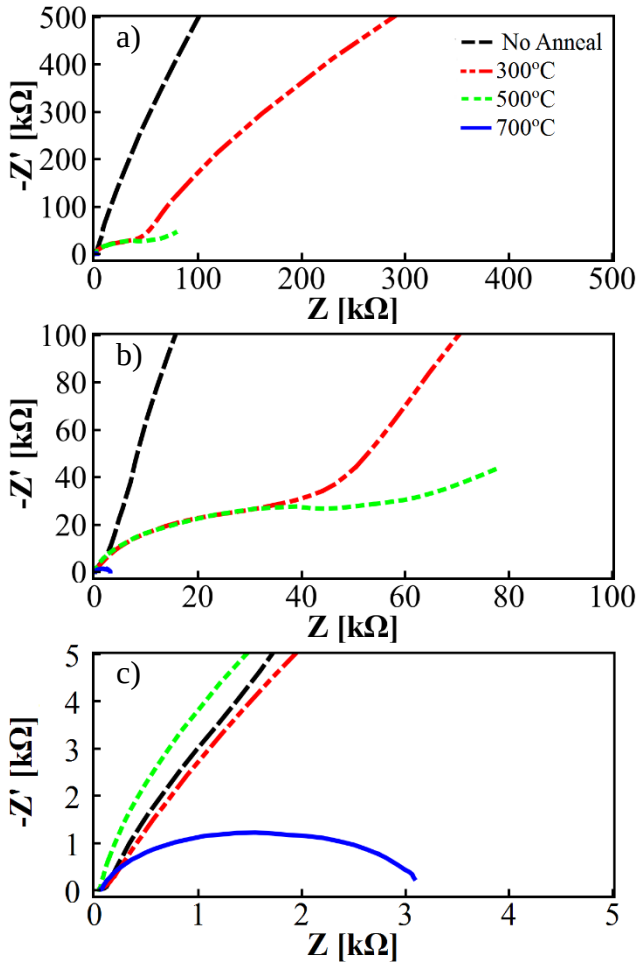

Figure 5. Nyquist plots of EIS measurements for STO films annealed at different temperatures. Figures 5.a-c show the same plots at different scales to clarify the large change.

Fitting EIS data with an equivalent electrical circuit can give insight into how the various elements of the system evolve. Here two equivalent circuits (see Figure 6) were fit to the data and compared. Fits with a single component circuit were compared to a dual component circuit where the additional component is associated with the space charge region of semiconductor electrodes [32–34]. The single component circuit was able to closely fit impedance from samples annealed at 500 ^{o}C and 700 ^{o}C but was not able to fit films annealed at lower temperatures. The second circuit was able to fit all samples (see Figure 7). For samples

annealed at high temperatures the calculated charge transfer resistance for each of these circuits was the same to within the uncertainty of the fit. Figure 6.c shows the resistance parameters for both circuits vary with annealing temperature. While the EIS curves appear to show only one component the relative ability of the two circuits to fit the impedance of the low temperature curves implies real effects that require additional parameters in the model [34]. Irrespective of the fit used, fits that worked well showed order of magnitude reductions in the characteristic

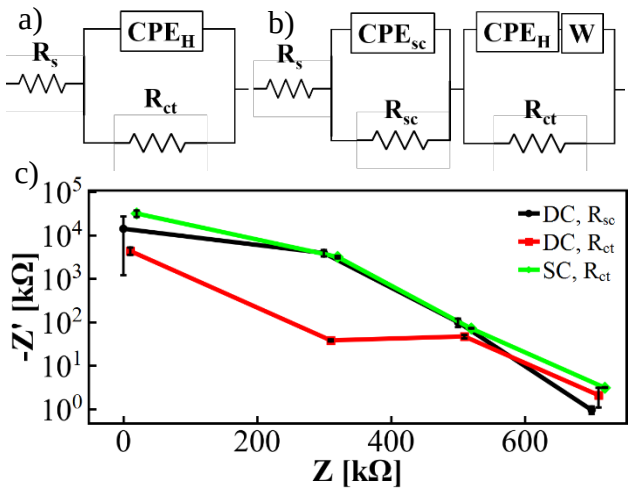

resistance of the films with higher annealing temperatures.

Figure 6. a) Single component equivalent circuit used for fitting EIS data. R_s – solution resistance, R_{ct} – charge transfer resistance, CPE_H – capacitance of Helmholtz layer. b) Dual component equivalent circuit used for fitting EIS data. R_{sc} – resistance of the space charge layer, CPE_{sc} – capacitance of space charge layer, W – Warburg impedance element. c) R_{sc} and R_{ct} are shown for STO electrodes annealed at different temperatures in a reducing environment (R_{ct} parameters are offset to make them more visible).

Changes in capacitance were insignificant relative to the large changes in both the space charge resistance (R_{sc}) and the interfacial charge transfer resistance (R_{ct}) thus the large increase

in photocurrent is attributed to the change in those two parameters (see Table 1 for values of all four parameters). Changes in R_{sc} are indicative of the increasingly crystalline STO film and its doping via annealing in a reducing environment. These changes correlate with previous measurements of STO in similar annealing conditions that showed increases in conductivity with annealing temperature [14,15]. Charge transfer resistance is a measure of how well charges move across the electrode/electrolyte interface. It is related to the charging of the Helmholtz layer and the relative positions of the semiconductor quasi-Fermi energy and the redox-Fermi level of the electrolyte. This EIS analysis does not allow a determination of what combination of properties changed to produce the effect seen here, rather it only provides a quantitative determination of the effective resistance associated with these parameters.

	R_{ct} (kΩ)	C_H (μF)	R_{sc} (kΩ)	C_{sc} (μF)
No Anneal	1.0×10^4	81	1.4×10^4	2.3
300 °C	38	1.4	3.7×10^3	15
500 °C	46	1.8	99	22
700 °C	1.9	9.9	1.0	5.7

Table 1. Values for charge transfer resistance, Helmholtz capacitance, space charge layer resistance, and space charge layer capacitance from dual component equivalent circuit model.

Reductions in charge transfer resistance for a PEC electrode are generally desirable but not always. If the charge transfer resistance is too low it can drastically increase the rate of charge recombination thereby reducing the performance of the cell. For this case, it is clear from the trend of increasing photocurrent with annealing temperature that any increase in charge

recombination is overshadowed by improvements in electrode performance due to improved charge injection and transfer to the conductive substrate.

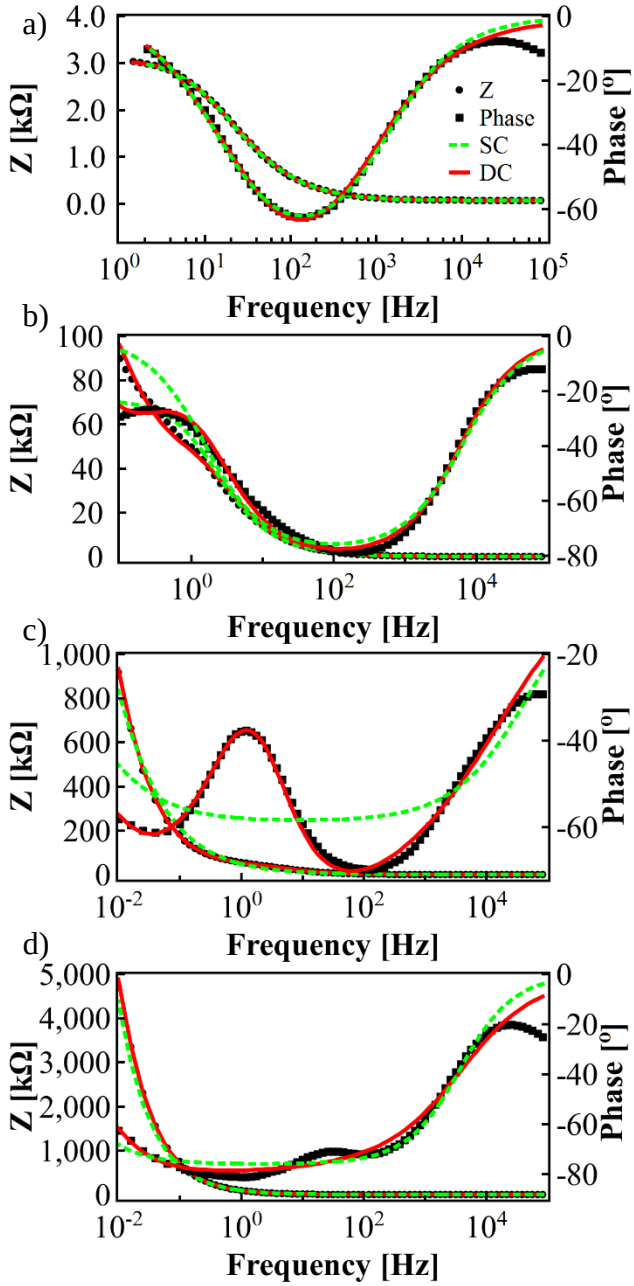

Figure 7. Bode plots of EIS data for samples annealed at a) 700 °C, b) 500 °C, c) 300 °C, and d) unannealed samples. Fits are done with the single component circuit (dashed, green line) and dual component circuit (solid, red line) shown in Figure 6.a and 6.b respectively.

Comparing the EIS and photocurrent data reveals a factor of 100 improvement – reduced impedance and increased photocurrent – between samples annealed at 500 °C and 700 °C. Conversely the lack of change in photocurrent between samples annealed at low temperatures does not correspond to the large change observed in the EIS data. Combining these observations with the optical measurements it appears that for well-ordered STO the improvements in photocurrent are due to the reduction in impedance that comes from the increase in donor states and conductivity. For the growth parameters used in this study, samples that were not annealed or annealed at 300 °C were not crystalline and therefore did not have the semiconductor band structure exhibited by films annealed at higher temperatures. Changes to the impedance and measured photocurrent of these non-crystalline samples must stem from a source distinct from the mechanism that causes impedance reductions and photocurrent improvements for films annealed at temperatures ≥ 500 °C.

3.4. Oxygen Measurements

PEC electrodes are often evaluated by considering the evolution of gaseous products from the reaction occurring at their interface. In the case of water-splitting the half reaction at the photoanode is the oxygen evolution reaction ($2H_2O \rightarrow O_2 + 4H^+ + 4e^-$). Following the technique used by Alibabaei et al. a modified RRDE setup was used to discern oxygen evolution by STO electrodes annealed at 700 °C [35]. The titanium substrate with a flat STO film was used as the disk electrode with a platinum ring electrode. In this setup products that evolve at the disk are forced across the ring electrode by rotating the disk. Products are detected at the ring electrode by a counter reaction (see Figure 8). In the case of oxygen evolution at the disk the oxygen is detected at the ring by a reductive reaction ($O_2+4H^+ +4e^- \rightarrow 2H_2O$). This strategy does not result in perfect collection at the ring, but confirms nevertheless the evolution of oxygen.

Figure 8 shows the disk and ring currents for applied voltages of 0.0 mV and -300 mV (vs. Ag/AgCl) respectively under periodic UV-illumination at a 750 Hz rotation frequency. The simultaneous currents appearing in the two plots illustrate that oxygen evolution is indeed occurring at these electrodes [36].

Faradaic efficiency of these measurements was strongly reliant on the disk current. Higher disk currents led to lower efficiencies indicating that for high disk currents more oxygen was made at the disk than could be reduced at the ring. For the lowest disk current measured for these samples (~10 μA) the I_{ring}:I_{disk} ratio was 0.95 (for maximum efficiency the applied voltages were V_{disk} = -200 mV vs. Ag/AgCl and V_{ring} = -300 mV vs. Ag/AgCl at 750 Hz rotation rate). Increased rotation rate also had a negative effect on Faradaic efficiency.

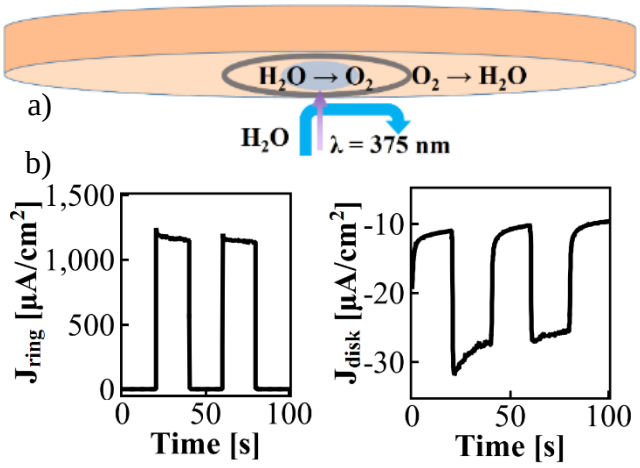

Figure 8. a) Schematic of RRDE setup. b) Sample curves for photocurrents at the disk and ring of the RRDE setup under illumination (V_{disk} = 0V vs. Ag/AgCl, V_{ring} = -300 mV Ag/AgCl, at 750 Hz rotation rate).

3.5. Porous Electrodes

A common method for improving PEC performance is to increase electrode surface area thereby scaling up the number of redox reactions occurring at the electrode-electrolyte interface and increasing total charge transfer. Films fabricated via PLD can be made more porous by increasing the chamber pressure during deposition. STO porous films were grown using an optimized back pressure based on previous work done with ITO porous films [37]. See Figure 9 for SEM images of porous films. The structure of these films was too delicate to use with the RRDE setup. Instead titanium substrates with STO films were attached to wires using a conductive epoxy. Flat film electrodes constructed with the wire electrode setup exhibited slightly less photocurrent than flat films in the RRDE setup due to an increase in contact resistance between the substrate and the external circuit.

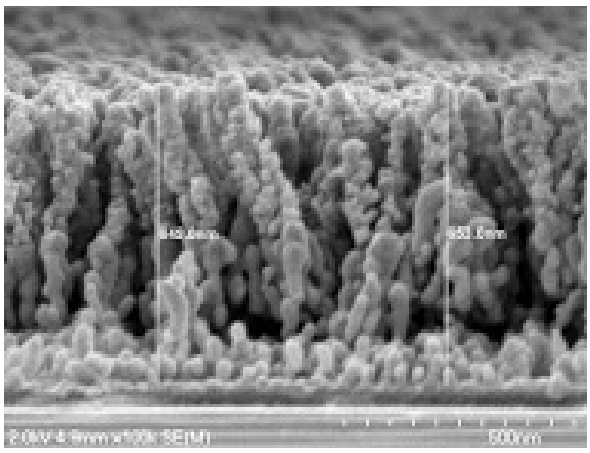

Figure 9. SEM image of porous films (side view). To see an SEM image of the flat film refer to SI for Call et al. [29].

Comparison of the photocurrents for the resulting films showed a 60 % improvement over flat films, see Figure 10.a. The difference in measured photocurrent between these two films did increase with higher applied potentials. Depositions on fused silica showed 5.0 % UV light

absorption for flat films (700 °C) and 6.7 % absorption for porous films (700 °C) at 375 nm. Because there is only a minor increase in absorption presumably the change in current comes from increased surface area due to a higher porosity. Qualitatively it appears that there is as much as a six-fold increase in surface area. Impedance spectroscopy data are shown in Figure 10.b for these films in the wire electrode setup. Since we are not able to quantify with precision the enhanced surface area at this moment, we can only speculate that perhaps the slight increase in impedance for porous films could prevent a linear improvement in photocurrent.

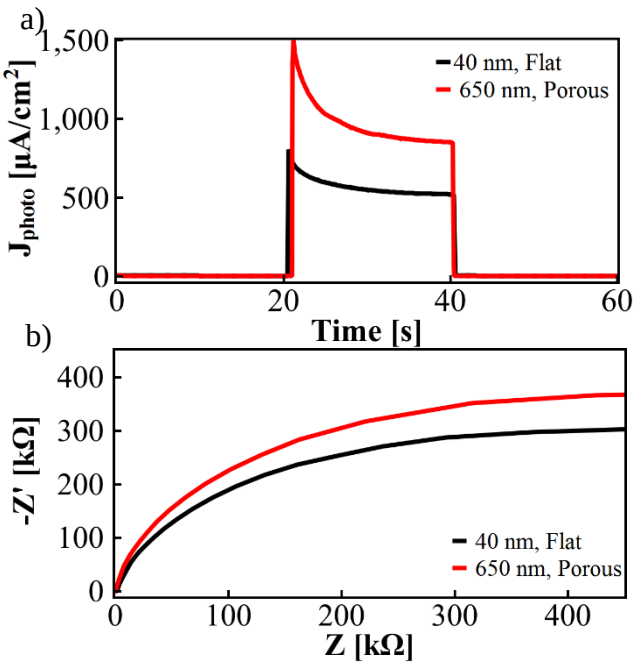

Figure 10. a) Photocurrent comparison of flat, dense STO film electrode and porous STO film electrode. b) EIS curves for non-illuminated porous and flat films using the wire-electrode assembly.

4. Conclusion

In this work STO electrodes for PECs were fabricated by deposition of STO films onto Ti substrates. The effects of post-deposition annealing on these electrodes were studied using

spectroscopic and electrochemical techniques. Optical measurements showed significant changes to films annealed at higher temperatures. XRD and spectroscopic ellipsometry showed increased crystallinity with higher annealing temperature. Higher annealing temperatures also led to extinction coefficient spectra that point to diminished optical bandgaps. Both observations are indicative of significant changes to the band structure of these films. Higher annealing temperatures led to substantially reduced impedance that contributes to improved electrode performance. This reduction in impedance is a result of decreased resistance at the electrode/electrolyte interface and in the space charge layer. The literature on STO suggests the mechanism for this change is the creation of both deep and shallow donor states in the crystalline films. This systematic characterization of annealing temperature effects on the photocatalytic activity of STO films directly shows how these material changes lead to improved performance.

Acknowledgements

This material is based upon work solely supported as part of the UNC EFRC: Center for Solar Fuels, and Energy Frontier Research Center funded by the U.S. Department of Energy, Office of Science, Office of Basic Energy Sciences under Award Number DE-SC0001011. Spectroscopic ellipsometry and pulsed laser deposition were performed at the Chapel Hill Analytical and Nanofabrication Laboratory (CHANL), a member of the North Carolina Research Triangle Nanotechnology Network (RTNN), which is supported by the National Science Foundation (Grant ECCS-1542015) as part of the National Nanotechnology Coordinated Infrastructure (NNCI). X-ray diffraction patterns (XRD) were collected at the Analytical Instrumentation Facility (AIF) at North Carolina State University, which is supported by the State of North Carolina and the National Science Foundation (award number ECCS-1542015). The AIF is a member of the North Carolina Research Triangle Nanotechnology Network (RTNN), a site in the

National Nanotechnology Coordinated Infrastructure (NNCI). We acknowledge Ching-Chang Chung (NC State) and (Tyler W. Farnsworth) for collecting XRD data.

References

[1] M.S. Wrighton, A.B. Ellis, P.T. Wolczanski, D.L. Morse, H.B. Abrahamson, D.S. Ginley, Strontium Titanate Photoelectrodes. Efficient Photoassisted Electrolysis of Water at Zero Applied Potential, J. Am. Chem. Soc. 98 (1976) 2774–2779.

[2] J.G. Mavroides, J. a. Kafalas, D.F. Kolesar, Photoelectrolysis of water in cells with SrTiO3 anodes, Appl. Phys. Lett. 28 (1976) 241–243. doi:10.1063/1.88723.

[3] A.B. Bocarsly, J.M. Bolts, P.G. Cummins, M.S. Wrighton, Photoelectrolysis of water at high current density: Use of ultraviolet laser excitation, Appl. Phys. Lett. 31 (1977) 568–570. doi:10.1063/1.89809.

[4] J. Yin, J. Ye, Z. Zou, Enhanced photoelectrolysis of water with photoanode Nb:SrTiO3, Appl. Phys. Lett. 85 (2004) 689–691. doi:10.1063/1.1775039.

[5] T. Arai, S. Sato, T. Kajino, T. Morikawa, Solar CO2 reduction using H2O by a semiconductor/metal-complex hybrid photocatalyst: enhanced efficiency and demonstration of a wireless system using SrTiO3 photoanodes, Energy Environ. Sci. 6 (2013) 1274–1282. doi:10.1039/c3ee24317f.

[6] M. Liu, J.L. Lyons, D. Yan, M.S. Hybertsen, Semiconductor-Based Photoelectrochemical Water Splitting at the Limit of Very Wide Depletion Region, Adv. Funct. Mater. 26 (2016) 219–225. doi:10.1002/adfm.201503692.

[7] S. Hara, H. Irie, Band structure controls of SrTiO3 towards two-step overall water splitting, Appl. Catal. B Environ. 115–116 (2012) 330–335. doi:10.1016/j.apcatb.2011.12.042.

[8] S. Hara, M. Yoshimizu, S. Tanigawa, L. Ni, B. Ohtani, H. Irie, Hydrogen and Oxygen Evolution Photocatalysts Synthesized from Strontium Titanate by Controlled Doping and Their Performance in Two-Step Overall Water Splitting under Visible Light, J. Phys. Chem. C. 116 (2012) 17458–17463. doi:10.1021/jp306315r.

[9] S. Kawasaki, K. Nakatsuji, J. Yoshinobu, F. Komori, R. Takahashi, M. Lippmaa, K. Mase, A. Kudo, Epitaxial Rh-doped SrTiO3 thin film photocathode for water splitting under visible light irradiation, Appl. Phys. Lett. 101 (2012) 33910. doi:10.1063/1.4738371.

[10] S. Kawasaki, R. Takahashi, K. Akagi, J. Yoshinobu, F. Komori, K. Horiba, H. Kumigashira, K. Iwashina, A. Kudo, M. Lippmaa, Electronic Structure and Photoelectrochemical Properties of an Ir-Doped SrTiO3 Photocatalyst, J. Phys. Chem. C. 118 (2014) 20222–20228.

[11] A.N. Pinheiro, E.G.S. Firmiano, A.C. Rabelo, C.J. Dalmaschio, E.R. Leite, Revisiting SrTiO3 as a photoanode for water splitting: development of thin films with enhanced charge separation under standard solar irradiation, RSC Adv. 4 (2014) 2029–2036. doi:10.1039/c3ra45066j.

[12] G. Li, Y. Bai, S. Wu, W. Zhang, Variation in Photocatalytic Activity of SrTiO3 (100) Single-Crystal Thin Films with Different Substrates and Annealing Atmosphere, Sci. Adv. Mater. 5 (2013) 764–768. doi:10.1166/sam.2013.1515.

[13] Y. Hikita, K. Nishio, L.C. Seitz, P. Chakthranont, T. Tachikawa, T.F. Jaramillo, H.Y. Hwang, Band Edge Engineering of Oxide Photoanodes for Photoelectrochemical Water Splitting: Integration of Subsurface Dipoles with Atomic-Scale Control, Adv. Energy

Mater. 6 (2016) 1502154. doi:10.1002/aenm.201502154.

[14] R.L. Wild, E.M. Rockar, J.C. Smith, Thermochromism and Electrical Conductivity in Doped SrTi O 3, Phys. Rev. B. 8 (1973) 3828–3835. doi:dx.doi.org/10.1103/PhysRevB.8.3828.

[15] B. Jalan, R. Engel-Herbert, T.E. Mates, S. Stemmer, Effects of hydrogen anneals on oxygen deficient SrTiO[sub 3−x] single crystals, Appl. Phys. Lett. 93 (2008) 52907. doi:10.1063/1.2969037.

[16] R. Waser, Solubility of Hydrogen Defects in Doped and Undoped BaTi03, J. Am. Ceram. Soc. 71 (1988) 58–63. doi:10.1111/j.1151-2916.1988.tb05760.x.

[17] A.E. Paladino, L.G. Rubin, J.S. Waugh, Oxygen ion diffusion in single crystal SrTiO3, J. Phys. Chem. Solids. 26 (1965) 391–397. doi:10.1111/j.1151-2916.1964.tb14416.x.

[18] L.C. Walters, R.E. Grace, Diffusion of point defects in strontium titanate, J. Phys. Chem. Solids 28 (1967) 245-248. doi:10.1016/0038-1098(66)90435-2.

[19] T. Tambo, K. Maeda, A. Shimizu, C. Tatsuyama, Improvement of electrical properties of epitaxial SrTiO3 films on Si(001)-2×1 by in situ annealing, J. Appl. Phys. 86 (1999) 3213–3217. doi:10.1063/1.371192.

[20] A. Kosola, M. Putkonen, L.S. Johansson, L. Niinistö, Effect of annealing in processing of strontium titanate thin films by ALD, Appl. Surf. Sci. 211 (2003) 102–112. doi:10.1016/S0169-4332(03)00175-2.

[21] B.G. Almeida, A. Pietka, J.A. Mendes, Thin Films Deposited by Laser Ablation Over Si Substrates, Integr. Ferroelectr. 63 (2004) 149–154. doi:10.1080/10584580490459297.

[22] S.W. Jiang, Q.Y. Zhang, Y.R. Li, Y. Zhang, X.F. Sun, B. Jiang, Structural characteristics of SrTiO3 thin films processed by rapid thermal annealing, J. Cryst. Growth. 274 (2005) 500–505. doi:10.1016/j.jcrysgro.2004.10.064.

[23] Y. Hu, O.K. Tan, J.S. Pan, H. Huang, W. Cao, The effects of annealing temperature on the sensing properties of low temperature nano-sized SrTiO3 oxygen gas sensor, Sensors Actuators B Chem. 108 (2005) 244–249. doi:10.1016/j.snb.2004.10.053.

[24] T.J. Park, J.H. Kim, J.H. Jang, J. Lee, S.Y.W. Lee, S.Y.W. Lee, H.S. Jung, C.S. Hwang, Effects of Annealing Environment on Interfacial Reactions and Electrical Properties of Ultrathin SrTiO3 on Si, J. Electrochem. Soc. 156 (2009) G129–G133. doi:10.1149/1.3152268.

[25] P. Pal, P. Kumar, A. V., A. Dogra, A.G. Joshi, Chemical potential shift and gap-state formation in SrTiO3−δ revealed by photoemission spectroscopy, J. Appl. Phys. 116 (2014) 53704. doi:10.1063/1.4892397.

[26] C.B. Samantaray, A. Dhar, D. Bhattacharya, M.L. Mukherjee, S.K. Ray, Effect of post-deposition annealing on microstructural and optical properties of barium strontium titanate thin films deposited by r . f . magnetron sputtering, J. Mater. Sci. Mater. Electron. 12 (2001) 365–370.

[27] N.B. Ibrahim, S.. Al-shomar, S.. Ahmad, Effect of Annealing Temperature on the Structural and Optical Properties of Nanocrystalline ZnO Thin Films Prepared by Sol-gel Method, Int. J. Innov. Res. Sci. Eng. Technol. 2 (2013) 1781–1786.

[28] M. EA, A. SM, B. YO, K. CD, Influence of Annealing Temperatures on the Structural, Morphological,Crystalline and Optical properties of BaTiO3 and SrTiO3 Nanoparticles, J.

Mater. Sci. Eng. 5 (2016) 3–8. doi:10.4172/2169-0022.1000277.

[29] R.W. Call, L. Alibabaei, R.J. Dillon, R.R. Knauf, A. Nayak, J.L. Dempsey, J.M. Papanikolas, R. Lopez, Growth and Post-Deposition Treatments of SrTiO3 Films for Dye Sensitized Photoelectrosynthesis Cell Applications, ACS Appl. Mater. Interfaces. 8 (2016) 12282-12290. doi:10.1021/acsami.6b01289.

[30] K. van Benthem, C. Elsässer, R.H. French, Bulk electronic structure of SrTiO[sub 3]: Experiment and theory, J. Appl. Phys. 90 (2001) 6156. doi:10.1063/1.1415766.

[31] M. Adachi, K. Noda, R. Tanino, J. Adachi, K. Tsuchiya, Y. Mori, F. Uchida, Comparison of Electrochemical Impedance Spectroscopy between Illumination and Dark Conditions, Chem. Lett. 40 (2011) 890–892. doi:10.1246/cl.2011.890.

[32] K. Chen, X. Feng, R. Hu, Y. Li, K. Xie, Y. Li, H. Gu, Effect of Ag nanoparticle size on the photoelectrochemical properties of Ag decorated TiO2 nanotube arrays, J. Alloys Compd. 554 (2013) 72–79. doi:10.1016/j.jallcom.2012.11.126.

[33] T. Lopes, L. Andrade, H.A. Ribeiro, A. Mendes, Characterization of photoelectrochemical cells for water splitting by electrochemical impedance spectroscopy, Int. J. Hydrogen Energy. 35 (2010) 11601–11608. doi:10.1016/j.ijhydene.2010.04.001.

[34] T. Lopes, L. Andrade, F. Le Formal, M. Gratzel, K. Sivula, A. Mendes, Hematite photoelectrodes for water splitting: evaluation of the role of film thickness by impedance spectroscopy, Phys. Chem. Chem. Phys. 16 (2014) 16515. doi:10.1039/C3CP55473B.

[35] L. Alibabaei, M.K. Brennaman, M.R. Norris, B. Kalanyan, W. Song, M.D. Losego, J.J. Concepcion, R.A. Binstead, G.N. Parsons, T.J. Meyer, Solar Water Splitting in a

Molecular Photoelectrochemical Cell, Proc. Nat. Acad. Sci. USA. 110 (2013) 20008–20013. doi:10.1073/pnas.1319628110/-/DCSupplemental.www.pnas.org/cgi/doi/10.1073/pnas.1319628110.

[36] J.J. Concepcion, R. a. Binstead, L. Alibabaei, T.J. Meyer, Application of the rotating ring-disc-electrode technique to water oxidation by surface-bound molecular catalysts, Inorg. Chem. 52 (2013) 10744–10746. doi:10.1021/ic402240t.

[37] T.R. Garvey, B.H. Farnum, R. Lopez, Pulsed laser deposited porous nano-carpets of indium tin oxide and their use as charge collectors in core–shell structures for dye sensitized solar cells, Nanoscale. 7 (2015) 2400–2408. doi:10.1039/C4NR05793G.